



Examination of occurrence probability of vortex-induced vibration of long-span bridge decks by Fokker–Planck–Kolmogorov equation

Wei Cui^{a,b,c}, Luca Caracoglia^d, Lin Zhao^{a,b,c,*}, Yaojun Ge^{a,b,c}

^a State Key Lab of Disaster Reduction in Civil Engineering, Tongji University, Shanghai 200092, China

^b Department of Bridge Engineering, College of Civil Engineering, Tongji University, Shanghai 200092, China

^c Key Laboratory of Transport Industry of Bridge Wind Resistance Technologies, Tongji University, Shanghai 200092, China

^d Department of Civil and Environmental Engineering, Northeastern University, 400 Snell Engineering Center, 360 Huntington Avenue, Boston, MA 02115, USA

ARTICLE INFO

Keywords:

Long span bridge

Vortex-induced vibration

Nonlinear aeroelastic model

VIV occurring probability

Fokker–Planck–Kolmogorov

Wind environment condition

ABSTRACT

Vortex-induced vibration (VIV) is a major concern for long-span bridge decks, which may happen especially for closed-box girders under certain environmental wind conditions. Traditionally, sustained VIV is observed as long as the wind speed falls within the lock-in region in wind tunnel tests. However, structural vibration monitoring of long-span bridges has indicated that frequency of VIV events may exhibit a probabilistic pattern. This paper proposes an analytical framework to evaluate the probability of VIV occurrence. First, a nonlinear aeroelastic model with multi-stability limit cycles is used to simulate the bridge deck VIV response within the VIV-triggering wind conditions. The first structural dynamic equilibrium point is usually unstable; the bridge deck instantaneous oscillation amplitude, which is excited by external environmental loads, must exceed this fixed point to trigger the VIV event. The external environmental excitation applied on bridge can be identified from the deck vibration without VIV occurring, then the VIV occurrence probability can be evaluated by Fokker–Planck–Kolmogorov equation. This study utilizes the field measurement data from the Humen Bridge, on which VIV event occurred the first time after 23-year servicing period, because water-filled barriers were placed along the two edges of bridge deck. Afterwards, VIV occurred frequently for over one month. The bridge deck VIV occurrence probability is evaluated by combining environmental wind information, stochastic deck excitation magnitude and a nonlinear aeroelastic VIV model. The results suggest that the proposed methods can approximate the VIV occurrence probability in comparison with empirical estimations using field measurements.

1. Introduction

1.1. Background on vortex-induced vibration of long-span bridge

Vortex-induced vibration (VIV) is one of the main concerns for long-span bridges, subjected to wind load effects. When airflow passes and separates around the bridge deck, vortices are alternately generated and periodically shed in the wake. Periodic vortex shedding produces variable pressures around the bridge deck. Cross-wind force and torque fluctuation is characterized by a predominant frequency described by the dimensionless Strouhal number $St = fD/U$, where f is the dominant frequency of vortex shedding; D is a characteristic dimension of the bridge deck; U is the mean incident flow velocity [1], directed orthogonally to the longitudinal bridge axis. Over the years, VIV events have been observed on several long-span bridge around the world, such as the Deer Isle Bridge in the USA [2], Great Belt Bridge in Denmark [3, 4], Trans-Tokyo Bay Crossing Bridge in Japan [5], Yi Sun-Sin Bridge in

Korea [6], Xihoumen [7,8] and Humen Bridges [9] in China. Because of the self-limiting load and vibration amplitude features, VIV of a bridge deck does not normally result in damage to structural elements. However, VIV disturbs bridge operations, causes discomfort to vehicles and pedestrians [9], and can lead to fatigue damage [10]. Compared to flutter, VIV happens at low-turbulence and lower wind speeds; it has therefore a much larger potential occurrence frequency than flutter, especially for closed-box deck girders. Therefore, VIV has recently become the main concern among wind-induced vibration phenomena for long-span bridges.

1.2. Recent challenges in the VIV modeling for long-span bridge

Understanding of VIV mechanisms is still an active research field, since it refers to rich and complex phenomena that have not been

* Correspondence to: Tongji University, 305 Wind Engineering Building, 1239 Siping Road, Shanghai, 200092, China

E-mail addresses: cuiwei@tongji.edu.cn (W. Cui), lucac@neu.coe.edu (L. Caracoglia), zhaolin@tongji.edu.cn (L. Zhao), yaojunge@tongji.edu.cn (Y. Ge).

Nomenclature

Symbols

A	Normalized vibration amplitude
A_*^i	i th order stationary vibration amplitude
$C(x)$	Damping matrix at bridge span x
C_k	Covariance matrix of Z_k
D	Bridge deck depth
$F(\cdot; x)$	Aeroelastic force function at bridge span x
F	Real part of F
G	Imaginary part of F
H_L	Hessian matrix
H_k	Spectral density matrix of the model response
I_i	i th order integral constant
I_{2n}	Identity matrix of $2n \times 2n$
$K(x)$	Stiffness matrix at bridge span x
L	Negative log-likelihood function
$M(x)$	Mass matrix at bridge span x
N	Number of samples per channel
N_q	Nyquist frequency
$P()$	Probability density function
S_{ij}	Cross spectral density
U	Mean wind speed
W	Standard Wiener process
Z_k	Vector of measured acceleration FFT
$f()$	Generalized aeroelastic force function in model coordinate
X	State vector in FPK equation
Y_1	Velocity dependent flutter derivative
Y_2	Motion dependent flutter derivative
a_i	i th order polynomial coefficient for $h(y/D)$
b_i	i th order polynomial coefficient for $g(\eta)$
$g(\eta)$	Normalized nonlinear aeroelastic damping function in terms of η
$h(y/D)$	Nonlinear aeroelastic damping function in terms of y/D
m	Generalized mass
s	Polynomial expansion order
t	Time
\hat{x}	Measured acceleration
x	Bridge deck location x
y	Generalized displacement by modal coordinate
$z(x)$	Vertical displacement at bridge span x
Δt	Sampling interval
F	FFT of \hat{x}_j
Φ	Mode shape matrix
$\Sigma_s(x)$	External excitation intensity at bridge span x
α	Wind skewed direction
β_{ij}	Frequency ratio
ϵ_a	Nonlinear aeroelastic damping coefficient
ϵ_j	Prediction error
η	Normalized motion in dimensionless time

i	Imaginary unit
ϕ	Vibration phase angle
$\psi(x)$	Mode shape function at deck location x
ρ	Air density
σ_s	Generalized external excitation intensity at bridge span x
θ	Model parameters
τ	Dimensionless time
μ	Nonlinear system function in FPK equation
ν	Angular vibration frequency
ω	Modal frequency
ξ	Damping ratio
FFT	Fast Fourier transform
FPK	Fokker–Planck–Kolmogorov
LCO	Limit-cycle oscillation
MPV	Most probable value
PDF	Probability density function
SDOF	Single-degree-of-freedom
SHM	Structural health monitoring
VIV	Vortex-induced vibration

vibration also has clear nonlinear features, such as the limit-cycle oscillation (LCO). The amplitude of LCO in the “lock-in” range depends, among others, on the wind speed. To model the nonlinear dynamics during “lock-in” range, several nonlinear dynamic models have been proposed. There are two categories of VIV dynamic models: the wake-oscillator model and the empirical, single-degree-of-freedom (SDOF) force model. The wake-oscillator model considers the vortex wake as an additional self-vibrating body, interacting with the structural oscillator in the wake region. The most famous models are Hartlen–Currie’s lift-oscillator model [11] and Iwan–Blevins’ early-wake model [12]. The SDOF-type models are also popular, especially in wind engineering, because it is based on an empirical relationship and it can be easily implemented. The SDOF model incorporates the vortex-induced force as a structural motion-dependent nonlinear aerodynamic force. The most famous SDOF model for bridge analysis is Scanlan’s nonlinear VIV model [13]; this model uses a quadratic term of the transverse displacement to modify aerodynamic damping effects, by reproducing self-limiting features using the van der Pol oscillator [14]. In recent years, several variants to Scanlan’s model and corresponding methods for coefficient identification have also been developed, such as direct aerodynamic measurements [15] and curve-fitting through instantaneous aerodynamic damping and stiffness [16].

However, most existing studies about VIV on bridges are based on the sectional model tests either in the wind tunnel or by computational fluid dynamics. The flow condition used by the two methods above is smooth; therefore the dynamic responses during VIV are deterministic. Nevertheless, in the atmospheric boundary layer, flow turbulence is present and the VIV is “disturbed” by the turbulence-induced random load effects. In current studies, random vibration effect has often been neglected by current methodologies since turbulence tends to reduce VIV vibration amplitudes. More importantly, VIV events on the actual bridge are probabilistic rather than deterministic [7]. Even under nearly identical environmental conditions, the VIV occurrence is uncertain. Difference in VIV occurrence probability between wind tunnel test and full-scale bridge is also not well documented in the existing literature.

1.3. Main objectives and anticipated outcomes of this study

This study proposes an integrated framework to evaluate the VIV response and its occurrence probability for long-span bridges subjected

fully understood. The mechanism of VIV fluid–structure interaction has been extensively investigated in the field of fluid mechanics. Because of the nonlinear aerodynamic flow instability, the structural

to low and moderate turbulence wind environments. First, a generalized van der Pol model is considered to evaluate the nonlinear VIV response for bridge decks with multi-stability patterns. Next, random vibration is described as an additive noise to the generalized van der Pol model. Therefore, the random vibration influence on VIV is simulated by a stochastic differential equation; Fokker–Planck–Kolmogorov (FPK) equation is employed to derive the VIV occurrence probability with various excitation intensity. This study employs the VIV response measurement from an actual long-span bridge that experienced frequent VIV events over a one-month periods. The structural dynamic parameters (frequency, damping and external excitation intensity) are identified by Bayesian inference from non-VIV random vibration data. The VIV-related aerodynamic parameters are calibrated from VIV response data. Finally, the VIV occurrence probability can be calculated according to the chain rule of conditional probability by combining the wind environment, external excitation and VIV probability evolution by FPK equation.

2. Stochastic modeling of bridge deck VIV influenced by external random excitation

2.1. Mathematical formulation of the nonlinear model

At the generic cross-section x along the bridge deck longitudinal axis, the governing equation of nonlinear, vortex-induced vibration is

$$M(x) \frac{d^2 z(x)}{dt^2} + C(x) \frac{dz(x)}{dt} + K(x)z(x) = F \left(\frac{dz(x)}{dt}, z(x); U \right) + \Sigma_s(x) \frac{dW}{dt} \quad (1)$$

where $z(x)$ is the vertical vibration of bridge deck at x , M , C and K are the structural mass, damping and stiffness coefficients, respectively; $F \left(\frac{dz(x)}{dt}, z(x); U \right)$ the fluid–structure interaction force during VIV at mean wind speed U . Additionally, the bridge is affected by noisy ambient excitation, which is represented by white noise of intensity as Σ_s ; W is a standard Wiener process, expressed in a “conventional” format to enable further derivation of the stochastic differential equation (although its derivative does not exist).

If single-mode VIV oscillation is considered and the frequencies of the deck bending modes are well-separated (i.e., a medium-span suspension bridge), the bridge deck motion can be presented by modal coordinate as $z(x) \approx y\psi(x)$. Therefore, the governing motion equation becomes

$$\frac{d^2 y}{dt^2} + 2\xi\omega_n \frac{dy}{dt} + \omega_n^2 y = f \left(\frac{dy(x)}{dt}, y(x); U \right) / m + \sigma_s \frac{dW}{dt} \quad (2)$$

where m is the modal mass calculated as $m = \int_0^l \psi^2(x)M(x)dx$, and l is the bridge deck span length; other quantities such as relative damping ξ , angular frequency $\omega_n = \sqrt{\frac{k}{m}}$ and ambient excitation σ_s can also be derived accordingly from Eq. (1).

According to Scanlan’s VIV model [13], the aeroelastic force f is

$$f \left(\frac{dy(x)}{dt}, y(x); U \right) = \rho U^2 D \left[Y_1 \left[1 - \epsilon_a \left(\frac{y}{D} \right)^2 \right] \frac{dy}{dt} U^{-1} + Y_2 \frac{y}{D} \right] \quad (3)$$

where ρ is the air density, Y_1 is the velocity dependent flutter derivative, Y_2 is the motion dependent flutter derivative and ϵ_a is the nonlinear aerodynamic damping coefficient.

Nevertheless, the previous equation describes a standard van–der–Pol oscillator with only one limit cycle, which cannot predict the VIV of bridge deck with multi-stability fixed points. Therefore, in this study, a novel nonlinear VIV model is proposed as

$$f \left(\frac{dy(x)}{dt}, y(x); U \right) = \rho U^2 D \left[Y_1 \left[1 - h \left(\frac{y}{D} \right) \right] \frac{dy}{dt} U^{-1} + Y_2 \frac{y}{D} \right] \quad (4)$$

in which $h \left(\frac{y}{D} \right)$ is a polynomial function of $\frac{y}{D}$ that describes nonlinear aerodynamic damping effects with Y_1 , $h \left(\frac{y}{D} \right) = \sum_{i=1}^N a_i \left(\frac{y}{D} \right)^i$. Previous

studies [17,18] have demonstrated $N = 6$ is sufficient to model the nonlinear aeroelastic force.

After normalization of wind speed and vibration frequency, the final dimensionless form of the proposed nonlinear VIV model can be re-written:

$$\ddot{\eta} + \epsilon [1 + g(\eta)] \dot{\eta} + \eta = \sigma \dot{W} \quad (5)$$

where the normalized motion $\eta = v^2 y/D$ and $\dot{}$ indicates differentiation with respect to dimensionless time $\tau = vU \frac{t}{D}$; v is the angular vibration frequency, accounting for structural aerodynamic stiffness effects with $v^2 = \left[\omega_n^2 \frac{D^2}{U^2} - m^* Y_2 \right]$; ϵ is the linear damping effect that combines structure and aeroelasticity $\epsilon = \left(2\xi\omega_n \frac{D}{U} - m^* Y_1 \right) v^{-1}$; the normalized nonlinear damping function is $g(\eta) = \sum_{i=1}^N b_i \eta^i$, with $b_i = a_i \frac{m^* Y_1}{\epsilon v^{2i}}$ and mass ratio $m^* = \rho D^2/m$. The external white noise intensity is $\sigma = \sigma_s v U D^{-1}$.

For vortex-induced vibration of bridge decks, the structural damping force and aeroelastic force are much smaller than the inertial force and stiffness restoring force; therefore Eq. (5) is a weakly nonlinear damping system and $|\epsilon| \ll 1$.

2.2. Amplitude and stability of multiple limit-cycle oscillation

Before analyzing the external noise effect on the VIV dynamics, the stability and multiple limit-cycle oscillation (LCO) amplitude should be studied by neglecting the noise term $\sigma \dot{W}$.

For a weakly nonlinear oscillator, the trajectories of above equation are nearly circular and can be defined as:

$$\begin{aligned} \eta &= A \cos(\tau + \phi) \\ \dot{\eta} &= -A \sin(\tau + \phi) \end{aligned} \quad (6)$$

where A is the non-negative amplitude, same as the one defined in the previous section, and ϕ is the phase.

Therefore, the squared amplitude can be found, and the differentiation yields

$$\begin{aligned} A^2 &= \eta^2 + \dot{\eta}^2 \\ \Rightarrow A\dot{A} &= \eta\dot{\eta} + \dot{\eta}\dot{\eta} = \eta\dot{\eta} + \dot{\eta} \{ -\eta - \epsilon\dot{\eta} [1 + g(\eta)] \} \\ &= -\epsilon\dot{\eta}^2 [1 + g(\eta)] = -\epsilon A^2 \sin^2(\tau + \phi) [1 + g(\eta)] \end{aligned} \quad (7)$$

Finally the temporal evolution of A is expressed as:

$$\dot{A} = -\epsilon A \sin^2(\tau + \phi) [1 + g(\eta)] = -\epsilon A \sin^2(\tau + \phi) \left[1 + \sum_{i=1}^s b_i A^i \cos^i(\tau + \phi) \right] \quad (8)$$

Because Eq. (5) has a weakly nonlinear damping term, the amplitude evolution is slowly varying and can be considered as constant during one vibration cycle. Therefore, the averaged amplitude evolution during one cycle is

$$\begin{aligned} \dot{A} &= -\frac{1}{2\pi} \epsilon A \int_{\tau-\pi}^{\tau+\pi} \sin^2(T + \phi) \left[1 + \sum_{i=1}^N b_i A^i \cos^i(T + \phi) \right] dT \\ &= -\frac{1}{2\pi} \epsilon A \left[\int_{\tau-\pi}^{\tau+\pi} \sin^2(T + \phi) dT \right. \\ &\quad \left. + \sum_{i=1}^N b_i A^i \int_{\tau-\pi}^{\tau+\pi} \sin^2(T + \phi) \cos^i(T + \phi) dT \right] \end{aligned} \quad (9)$$

When index i is odd, the above integral over one period is 0. Therefore, the terms with even i are only kept in the above formula. Consequently, the temporal variation of vibration amplitude is rewritten as:

$$\dot{A} = -\epsilon A \left[I_0 + \sum_{i=1}^{N/2} b_{2i} I_{2i} A^{2i} \right] \quad (10)$$

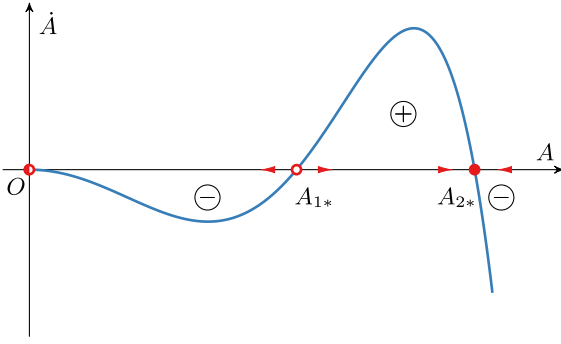


Fig. 1. Conceptual sketch of amplitude evolution for VIV with multiple limit cycles (legend: \circ , unstable equilibrium; \bullet , stable LCO; \odot , neutral point; \rightarrow , amplitude evolution direction; \ominus , energy decays; \oplus , energy increases).

where

$$I_0 = \frac{1}{2\pi} \int_{\tau-\pi}^{\tau+\pi} \sin^2(T + \phi) dT = \frac{1}{2} \quad (11a)$$

$$I_{2i} = \frac{1}{2\pi} \int_{\tau-\pi}^{\tau+\pi} \sin^2(T + \phi) \cos^{2i}(T + \phi) dT = \frac{2i-1}{2i+2} I_{2i-2} \quad (11b)$$

When the dynamic system enters a limit cycle with amplitude A_* , $\dot{A} = 0$, and

$$I_0 + \sum_{i=1}^{N/2} b_{2i} I_{2i} A_*^{2i} = 0 \quad (12)$$

In other words, A_*^2 is the root of above formula.

For the scenario $\epsilon > 0$, i.e. structural damping is larger than the linear part of the aerodynamic damping effect, there are at least two positive roots A_{1*}^2 and A_{2*}^2 . The conceptual sketch of amplitude evolution is plotted in Fig. 1.

When the amplitude A is smaller than A_{1*} , the \dot{A} is negative. In this situation, the structure cannot develop a stable amplitude since A is unable to exceed A_{1*} . By contrast, the amplitude A is larger than A_{1*} , and the \dot{A} is positive and approaches A_{2*} . If the amplitude A is larger than A_{2*} , the \dot{A} is also negative and tends to A_{2*} . In summary, A_{1*} is an unstable equilibrium point, and A_{2*} is a stable equilibrium point. Consequently, the initial amplitude A must exceed A_{1*} to trigger VIV.

2.3. Determination of VIV model coefficients

Either field measurements of bridge vibration or aeroelastic section model of the bridge deck in wind tunnel can be used. The first step is mean wind speed and vibration frequency normalization described in Eq. (5). During VIV, v can be measured from the predominant vibration frequency. For the aeroelastic section model of the bridge deck, the mass m , ξ and ω_n can easily be determined in the laboratory. However, it is difficult to identify these structural-dynamic coefficients for the full-scale bridge.

Assuming that m , ξ and ω_n and v are known, vibrations can be re-scaled into dimensionless form in Eq. (5). The remaining aerodynamic coefficients ϵ and b_i can be found from the amplitude evolution formula in Eq. (10).

The amplitude evolution $A(\tau)$ can be derived by Hilbert transform of $\eta(\tau)$. On the other hand, the simulated VIV amplitude $\hat{A}(\tau)$ is calculated by time integration from Eq. (10) if ϵ and b_{2i} are known. Thus, ϵ and b_{2i} can be determined by minimizing the difference between $A(\tau)$ and $\hat{A}(\tau)$. The procedure can be expressed as a mathematical optimization

$$\arg \min_{\epsilon, b_{2i}} |A(\tau) - \hat{A}(\tau)| \quad (13)$$

3. Identification of structural dynamic properties by Bayesian FFT method

Modal frequencies and damping ratios are two important parameters to predict bridge VIV and to enable the normalization of Eq. (5),

which are required to identify aeroelastic parameters and VIV occurrence probability. Structural health monitoring (SHM) [19] can provide sufficient information about the full-scale structure and external excitation as to infer structural dynamic properties.

An efficient algorithm was developed to identify the most probable value (MPV) and corresponding variance-covariances properties of the modal properties (e.g., modal frequencies and damping ratios) for bridge decks with both well-separated and closely-spaced modes [20] and [21]. In this section, the definitions of some quantities have been adapted from the original formulation. If the acceleration time history is digitally measured at n DOFs of a structure and is denoted as $\{\hat{x}_j \in \mathbb{R}^n : j = 1, \dots, N\}$ or $\{\hat{x}_j\}$, with N being the number of samples per channel, the FFT of $\{\hat{x}_j\}$ is defined as

$$F_k = F_k + iG_k = \sqrt{(2\Delta t)/N} \sum_{j=1}^N \hat{x}_j \exp\{-2\pi i[(k-1)(j-1)/N]\} \quad (k = 1, \dots, N) \quad (14)$$

where $i^2 = -1$; Δt is the sampling interval; $F_k = \text{Re } F_k$ and $G_k = \text{Im } F_k$ denote the real and imaginary part of the FFT, respectively. For $k = 2, 3, \dots, N_q$, the FFT corresponds to frequency $f_k = (k-1)/N\Delta t$. Here, $N_q = \text{int}[N/2] + 1$ ($\text{int}[\cdot]$ denotes the integer part) corresponds to the FFT ordinate at the Nyquist frequency. For modal identification only, these $(N_q - 1)$ FFT values are utilized.

In the context of Bayesian inference, the measured acceleration is modeled as $\hat{x}_j = x_j(\theta) + \epsilon_j$ where $x_j(\theta)$ is the acceleration response of the structural model, defined by the set of model parameters θ ; ϵ_j is the prediction error that accounts for the deviation between the modeled response and measured data, possibly owing to measurement noise and modeling error.

The joint probability density function (PDF) of the augmented FFT vectors [20] is derived as $\{Z_k = [F_k^T, G_k^T]^T \in \mathbb{R}^{2n} : k = 2, \dots, N_q\}$ and it is applied to Bayesian modal identification. For a high-sampling-rate and long-duration record, Z_k is a zero-mean Gaussian vector with variance-covariance matrix given by [20]

$$C_k = \frac{1}{2} \begin{bmatrix} \Phi(\text{Re } H_k) \Phi^T & -\Phi(\text{Im } H_k) \Phi^T \\ \Phi(\text{Im } H_k) \Phi^T & \Phi(\text{Re } H_k) \Phi^T \end{bmatrix} + (\sigma^2/2) I_{2n} \quad (15)$$

where $\Phi \in \mathbb{R}^{n \times m}$ is the mode shape matrix, discretized using the measured DOFs (the i th column coincides with the i th deck mode shape); σ^2 is the (constant) spectral density intensity of the white-noise prediction error; I_{2n} denotes the $2n \times 2n$ identity matrix; H_k is the spectral density matrix of the model response with (i, j) entry given by

$$H_k(i, j) = S_{ij} [(\beta_{ik}^2 - 1) + i(2\xi_i \beta_{ik})]^{-1} [(\beta_{jk}^2 - 1) - i(2\xi_j \beta_{jk})]^{-1} \quad (16)$$

where $\beta_{ik} = f^{(i)}/f_k$ = frequency ratio; $f^{(i)}$ and ξ_i are natural frequency and damping ratio of the i th mode, respectively; S_{ij} is the cross spectral density between the i th and j th modal excitation, which is related to the ambient excitation intensity σ_s .

The set of modal parameters θ consists of modal frequencies, damping ratios, mode shapes, entries $\{S_{ij}\}$ of the spectral density matrix of the modal excitation and spectral density of the prediction error. Assuming a non-informative prior distribution, the posterior PDF of θ given the FFT data is proportional to the likelihood function $p(\{Z_k\}|\theta)$

$$p(\theta|Z_k) \propto p(Z_k|\theta) = (2\pi)^{-\frac{N_q-1}{2}} \left[\prod_{k=2}^{N_q} \det C_k(\theta) \right]^{-\frac{1}{2}} \exp \left[-\frac{1}{2} \sum_{k=2}^{N_q} Z_k^T C_k(\theta)^{-1} Z_k \right] \quad (17)$$

where the dependence of C_k on θ has been emphasized [22]. It is convenient to use the negative log-likelihood function $L(\theta)$ form

$$p(\theta|Z_k) \propto \exp[-L(\theta)] \quad (18)$$

where

$$L(\theta) = \frac{1}{2} \sum_{k=2}^{N_q} [\ln \det C_k(\theta) + Z_k^T C_k(\theta)^{-1} Z_k] \quad (19)$$

With a sufficiently large amount of data, the posterior PDF is equivalent to second-order approximation of $L(\theta)$. Specifically, let $\hat{\theta}$ be the MPV that minimizes L and consider the second-order Taylor series about $\hat{\theta}$

$$L(\theta) \approx L(\hat{\theta}) + \frac{1}{2}(\theta - \hat{\theta})^T H_L(\hat{\theta})(\theta - \hat{\theta}) \quad (20)$$

and where the first-order term vanishes because of optimal $\hat{\theta}$; $H_L(\hat{\theta})$ is the Hessian of L at MPV. Substituting into Eq. (18), the posterior PDF becomes a Gaussian PDF

$$p(\theta|Z_k) \propto \exp \left[-\frac{1}{2}(\theta - \hat{\theta})^T \hat{C}^{-1}(\theta - \hat{\theta}) \right] \quad (21)$$

where

$$\hat{C} = H_L(\hat{\theta})^{-1} \quad (22)$$

is the posterior variance-covariance matrix.

MPVs of modal properties can be determined by minimizing $L(\theta)$. Practically, numerical issues are inevitable while calculating the inverse of the variance-covariance matrix C_k , which can be solved as explained by [21].

It should be noted that, in this study, the MPVs of structural dynamic properties are employed to predict the VIV response. Their uncertainties are not considered in this study.

4. VIV occurrence probability for long-span bridges by FPK equation

4.1. Evaluating the VIV occurrence probability by FPK equation

If the nonlinear VIV model and external excitation are jointly considered, the nonlinear VIV model can be rewritten as a two-dimensional stochastic differential equation

$$dX = \mu(X, \tau) d\tau + \sigma dW \quad (23)$$

where

$$X = \begin{bmatrix} \eta \\ \dot{\eta} \end{bmatrix} \quad (24a)$$

$$\mu(X, \tau) = \begin{bmatrix} \dot{\eta} \\ -\eta - \epsilon \dot{\eta} [1 + g(\eta)] \end{bmatrix} \quad (24b)$$

$$\sigma = \begin{bmatrix} 0 \\ \sigma \end{bmatrix} \quad (24c)$$

The probability density evolution $p(X, \tau)$ satisfies the Fokker-Planck-Kolmogorov equation [23]:

$$\frac{\partial p(X, \tau)}{\partial \tau} = - \sum_{i=1}^2 \frac{\partial}{\partial X_i} [\mu_i(X, \tau) p(X, \tau)] + \sum_{i=1}^2 \sum_{j=1}^2 \frac{\partial^2}{\partial X_i \partial X_j} [D_{ij} p(X, \tau)] \quad (25)$$

$$\text{where } D = \frac{1}{2} \sigma \sigma^T = \frac{1}{2} \begin{bmatrix} 0 & 0 \\ 0 & \sigma^2 \end{bmatrix}.$$

FPK equations have been widely used to study various engineering systems, such as stability analysis [24] and non-stationary excitation [25]. In this study, finite difference numerical methods are employed to solve the FPK equation. In recent years, there are several advanced computational methods to solve FPK equation [26]. Since there are only two DOF involved in this study, the classic alternating direction methods are employed to accelerate the computation [27].

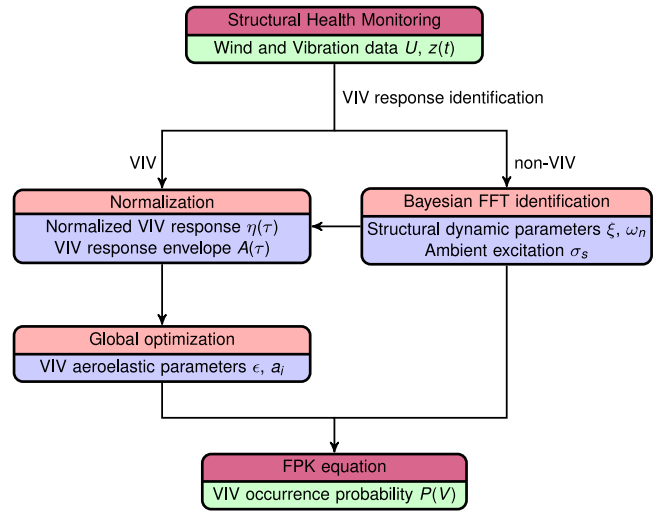


Fig. 2. Flowchart for estimation of VIV occurrence probability (top panel: methodology; bottom panel: results).

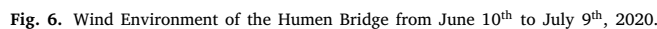
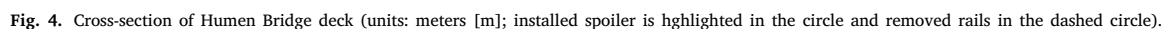


Fig. 3. Geographic location of Humen Bridge.

4.2. Summary flowchart of the proposed framework

This study proposes a framework to calculate the VIV occurrence probability, integrating the methodologies listed in the previous sections. An engineering application example will be presented, based on the SHM system installed on a long-span bridge, which experienced frequent VIV. First, the structural vibration data is separated into VIV and non-VIV records. The structural dynamic parameters, such as frequency and damping, can be identified from non-VIV data by Bayesian FFT technique. Substituting the modal frequency and damping into the VIV data, the normalized VIV responses $\eta(\tau)$ and amplitude evolution $A(\tau)$ can be derived. Subsequently, the VIV-related aeroelastic parameters are identified by optimization. At last, combining the VIV nonlinear dynamic model with identified ambient excitation intensity, the VIV occurrence probability conditional on specific mean wind speed, direction and ambient intensity can be found by FPK equation. The procedure described above is summarized in Fig. 2 that summarizes each step of the methodology with corresponding outcomes.

Finally, the total VIV occurrence probability is found by the chain rule of marginal probability of mean wind speed, direction, ambient excitation intensity distribution and conditional VIV occurrence



In the previous equation $P(V)$ is the total VIV occurrence probability, $P(U, \alpha)$ is the joint probability distribution of mean wind speed U and wind yaw direction angle, measured orthogonally to bridge deck axis, α ; $P(\sigma_s|U, \alpha)$ is the probability distribution of ambient excitation intensity for specific U and α , $P(V|U, \alpha, \sigma_s)$ is the conditional probability distribution calculated by FPK equation.

The VIV events on Humen Bridge are employed. Unexpected VIV events that occurred on the Humen Bridge deck starting from May 5th, 2020 [9]. To monitor the status of the Humen Bridge, an SHM system

In the beginning, to suppress VIV on Humen Bridge, spoilers were installed at the top of handrails [9], as highlighted in the solid circle of Fig. 4. The VIV response amplitudes were decreased but not completely suppressed. From early July 2020, the rails at two ends of the deck

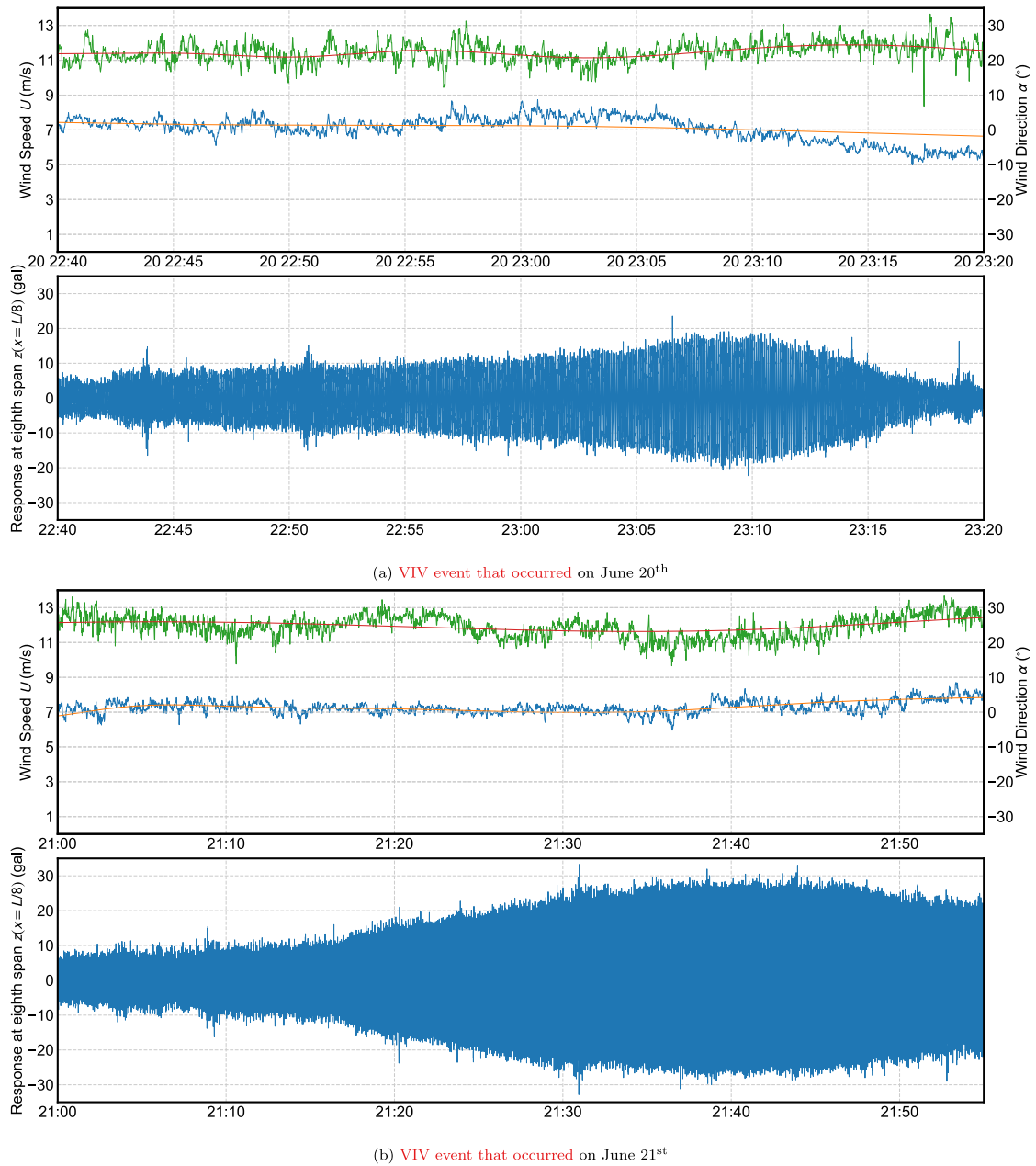


Fig. 7. VIV events with and without stable LCO.

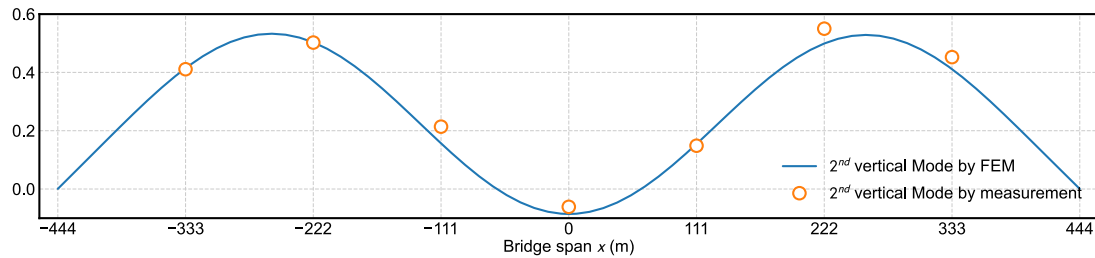


Fig. 8. The 2nd symmetric vertical bending deck mode shape, identified by response measurements and finite element methods.

bottom were removed, after which the VIV response was entirely eliminated [28]. One-month period records from June 10th to July 9th, during which the spoiler and rails were still installed on the bridge deck, were employed in this study.

The SHM system on the Humen Bridge includes three-dimensional ultrasonic anemometers and unidirectional accelerometers. The anemometers are used for wind-speed monitoring at a sampling frequency $f_s = 4$ Hz (purple points shown in Fig. 5). On the middle

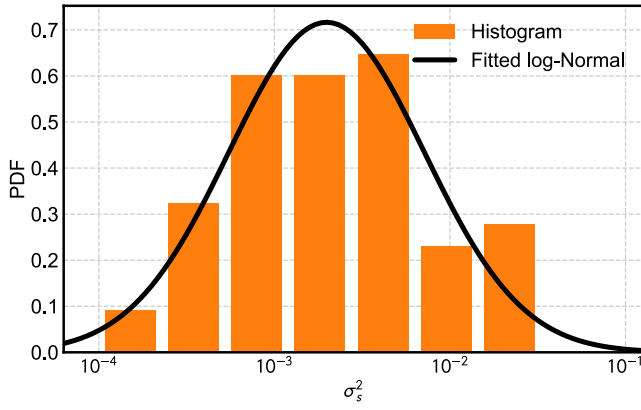


Fig. 9. Empirical distribution and fitted PDF of external excitation intensity σ_s .

main span, one group of three-dimensional anemometers are installed on both sides to avoid aerodynamic interference. The incoming flow always carries fluctuating turbulent winds, even in VIV events. Seven sections (each eighth point) were selected for bridge deck vibration monitoring; 14 unidirectional accelerometers (vertical only) were arranged with sampling frequency $f_s = 50$ Hz (green points shown in Fig. 5). The sensor layout is shown in Fig. 5.

5.1. Wind environment and joint PDF of mean wind speed and direction

During the one-month period, 10-min averaged wind speeds and directions are described in Fig. 6. Fig. 6(a) shows the wind rose graph in percentage with the bridge span and bridge normal directions indicated as references. It clearly indicates that, during the monitoring period, most wind directions are only slightly skewed from the axis orthogonal to bridge deck, which is a promotive condition for VIV. Utilizing the observed data, an angular-linear probability distribution [29–31], composed of Weibull and von Mises distributions, was employed to find the joint PDF $P(U, \alpha)$ of mean wind speed and direction at deck height; the fitted $P(U, \alpha)$ is shown as contour plots in Fig. 6(b).

Besides mean wind speed and direction, turbulence intensity is another important VIV-related factor. Since the wind directions are confined to a small wind rose sector, and the wind exposure is open sea, turbulence intensity was measured around 5%, low and promotive to VIV.

5.2. Description of VIV events on the human bridge deck

VIV events were identified and separated from other vibration events (e.g. vehicle-induced vibration and buffeting). The vehicle-induced vibration and buffeting are typical broadband stochastic processes with multiple modes. By contrast, the characteristics of VIV are single frequency simple harmonic vibration, and the root-mean-square of acceleration response is generally larger than other vibrations. Based on the acceleration response measurements on the bridge deck, the two features are employed to separate VIV from other vibrations [32].

From June 10th to July 9th, there were 28 VIV events. However, because of non-stationary wind conditions, some VIV events did not lead to stable deck LCO. For example in Fig. 7(a), the VIV event on June 20th started from 22:40 and the bridge response amplitude kept on growing; however, after 23:10, the wind speed decreased to around 5 m/s and the VIV amplitude started to decrease. Had the wind conditions been stable for a longer duration, the bridge deck response would have reached an LCO with nearly constant amplitudes, such as Fig. 7(b). There were 12 VIV events that lead to a stable LCO out of 28 observed events, and used herein.

From the wind environments corresponding to the 28 VIV events, the 10-minute mean wind speed was $6.5 \leq U \leq 8.0$ m/s and the mean wind direction was $-5 \leq \alpha \leq 25^\circ$. From June 10th to July 9th, there were total 54 nonconsecutive time periods, during which mean wind speed and direction fell within the VIV-triggering conditions. The vibration frequencies of VIV events are all around 0.22–0.23 Hz, plausibly influenced by aerodynamic stiffness effect. The VIV deck mode is the second symmetric vertical bending deck mode, which is plotted in Fig. 5. If the acceleration threshold for VIV occurrence was set to 10 gal (0.048 m converted to typical modal displacement), only 28 out of 54 records triggered the VIV events. This remark clearly demonstrates that VIV occurrence is probabilistic rather than deterministic, even during promotive wind conditions.

5.3. Structural dynamic properties and external excitation intensity identified by Bayesian FFT approach

Non-VIV vibrations data were used to identify the structural dynamic properties. To minimize the interference from aerodynamic damping and stiffness, as well as the traffic, records of deck vibration corresponding to mean wind speed smaller than 2 m/s and local time from 0:00 to 6:00 were employed in the identification. Based on the Bayesian FFT approach described in Section 3, the vibration frequency of the second symmetric vertical bending mode of the deck, excited by VIV events, is 0.2284 Hz and the corresponding modal damping is 0.27%. There exists randomness in the identification of structural dynamic properties, especially damping. However, because the vibration data were pre-selected by low wind conditions and night time, uncertainty in structural frequency is not significant. Therefore, constant structural frequency was considered in this study. On the other hand, structural damping is critical for VIV aeroelastic modeling. In the proposed model damping is determined as one coefficient ϵ , combining the structural with the linear part of aeroelastic damping effect. Thus, uncertainty in estimation of structural damping was merged with aeroelastic parameter identification in Eq. (13).

Before the identification of external excitation, the VIV-related mode shape should also be identified and explicitly defined to regulate the quantities of the external excitation, σ_s . The mode shape normalization is defined as

$$\sqrt{\sum_i \psi_i^2(x)} = 1 \quad (27)$$

where the ψ_i is the response of the i th sensor placed along the bridge deck. The mode shape of the 2nd symmetric vertical bending deck mode, identified by Bayesian FFT approach, is plotted in Fig. 8. The mode shape, calculated by finite element methods according to the Humei Bridge structural design information, is also plotted for comparison purposes.

The external excitation intensity, identified by the Bayesian FFT methods, has a much larger variance, which may be plausibly affected by wind turbulence as well as other excitation sources including traffic and wave loading transferred from the ground.

Bridge vibration data during wind events promotive to VIV were used ($6.5 \leq U \leq 8.0$ m/s and $-5 \leq \alpha \leq 25^\circ$) to identify ambient excitation intensity. Furthermore, since the VIV-triggering conditions only contain a small wind speed range with very limited contribution of turbulence-induced random force, the PDF of the ambient excitation is uniform for the whole VIV-triggering condition. In order words, $P(\sigma_s|U, \alpha) = P(\sigma_s)$

As stated in the previous section, there were 54 nonconsecutive time periods falling within the suitable range, twenty-six of which were non-VIV events with duration between 20 min and 90 min. These 26 nonconsecutive events were divided into 84 uniform-length segments of 10 minute duration. The Bayesian FFT approach was used again to identify external excitation intensity σ_s ; the empirical histogram of σ_s is plotted in Fig. 9 after normalization of the total area of the histogram

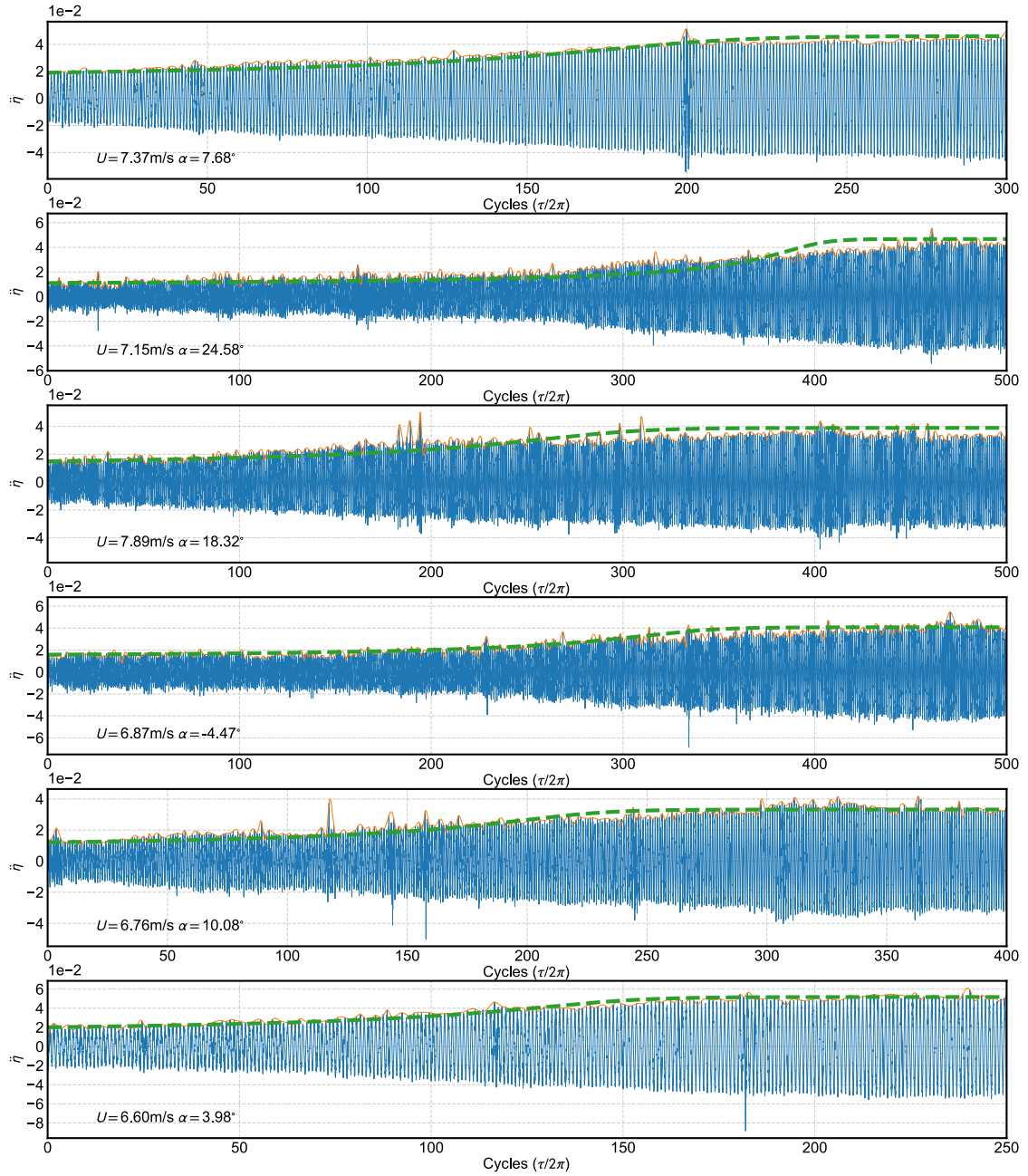
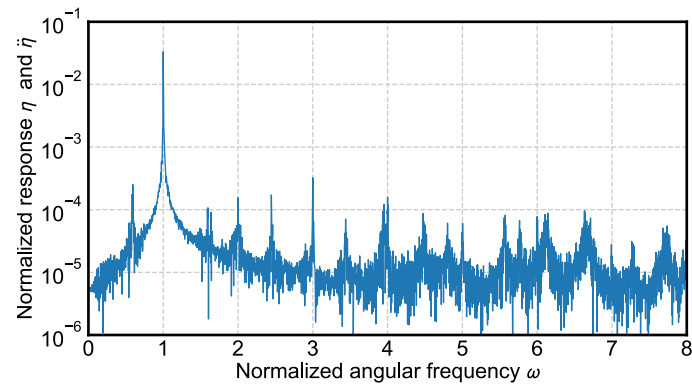


Fig. 10. Six VIV events exhibiting stable LCO.

Fig. 11. Amplitude spectrum of VIV response η .

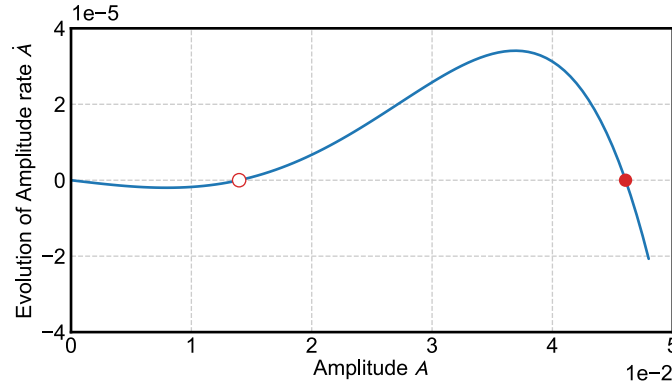


Fig. 12. Evolution of amplitude “rate” \dot{A} using aeroelastic parameters identified from the first VIV event in Fig. 10.

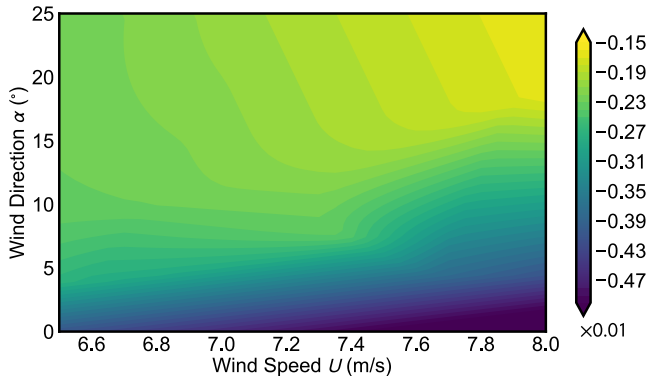


Fig. 13. Contour plot of net damping ϵ , with wind field environment suitable to VIV.

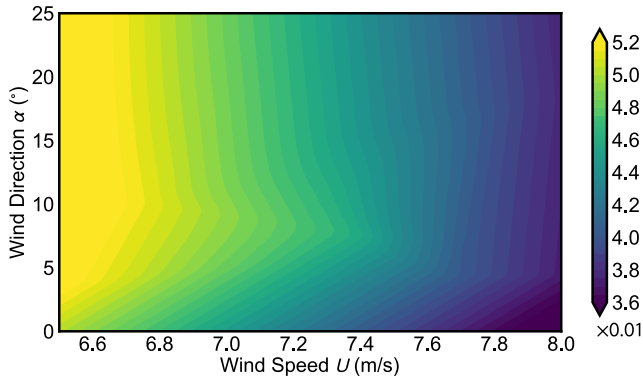


Fig. 14. Contour plot of stable LCO amplitude, with wind environment suitable to VIV.

to one. A log-normal PDF model was utilized to fit the histogram as the $P(\sigma_s)$ in this study; very good match can be found in the figure.

5.4. Determination of VIV aeroelastic parameters from vibration measurements

After the determination of structural frequency and damping, vibration measurements can be converted to dimensionless format as in Eq. (5). The angular vibration frequency ν can be found from the predominant acceleration frequency in the signals.

Fig. 10 presents six VIV events being able to reach a stable LCO stage. The dimensionless time is scaled to $\tau/2\pi$ as to normalize unit value to one period. The Fourier transform of the acceleration signal from the first VIV event is plotted in Fig. 11. Because the angular frequency is 1, therefore the spectrum of displacement η and acceleration

$\ddot{\eta}$ are exactly the same. It clearly shows that the unit-value frequency component dominates the response; this condition greatly simplifies the identification of the aeroelastic parameters.

As stated in Section 2.3 and flow chart in Fig. 2, the amplitudes evolution during VIV events can be determined by the Hilbert transformation and plotted as orange line in Fig. 10. Next, the aeroelastic parameters can be identified through minimizing the difference between the calculated amplitude evolution in Eq. (10) and measurements. Furthermore, because the LCO amplitudes A_* are known from Fig. 10, thus the aeroelastic parameters must satisfy Eq. (12). After all, the aeroelastic parameters can be summarized as a constrained optimization problem as:

$$\begin{aligned} & \arg \min_{\epsilon, A_{i*}} |A(\tau) - \hat{A}(\tau)|, \\ & \text{subject to: } I_0 + \sum_{i=1}^{N/2} b_{2i} I_{2i} A_{i*}^{2i} = 0; \end{aligned} \quad (28)$$

Taking the first VIV event in Fig. 10 as an example, the amplitude “rate” \dot{A} can be calculated by Eq. (10). Because the net damping $\epsilon > 0$, the initial \dot{A} at smaller amplitudes is negative; thus, at this stage, the structural response tends to decay to 0. As A becomes larger, the nonlinear aeroelastic force drastically increases to balance the net damping ϵ effect. At $A \approx 0.14$, \dot{A} is zero (marked by a hollow circle in Fig. 12), but \dot{A} is positive; thus, A starts to grow when A exceeds this unstable equilibrium point. After that, the nonlinear aeroelastic force gradually increases, and the second point with $\dot{A} = 0$ appears as the stable LCO (marked by a solid circle in Fig. 12) and the VIV amplitude is observed.

By examining Fig. 12, it can be deduced that the deck always vibrates around the equilibrium point at 0, and the structural response must exceed the unstable equilibrium point to activate the aeroelastic force and promote stable VIV. Even if the wind field environment is suitable to VIV, VIV occurrence depends on the instantaneous random amplitude that must exceed the unstable equilibrium point; therefore, occurrence is probabilistic rather than deterministic.

After aeroelastic parameter identification, amplitude evolution can be simulated numerically and plotted as the dashed line in Fig. 10. Good correspondence is noted between simulations and measurements, demonstrating the suitability of the nonlinear VIV model proposed in this study.

Utilizing all 28 VIV events, the aeroelastic parameters for VIV-triggering wind environment $6.5 \leq U \leq 8.0 \text{ m/s}$ and $-5^\circ \leq \alpha \leq 25^\circ$ are identified; the interpolation of ϵ and amplitudes of stable LCO are plotted as contours in Figs. 13 and 14. Because of the symmetry along the bridge deck’s normal direction, the parameters are the same for both $\alpha < 0$ and $\alpha > 0$. The results and figures related to other model parameters are omitted for the sake of brevity.

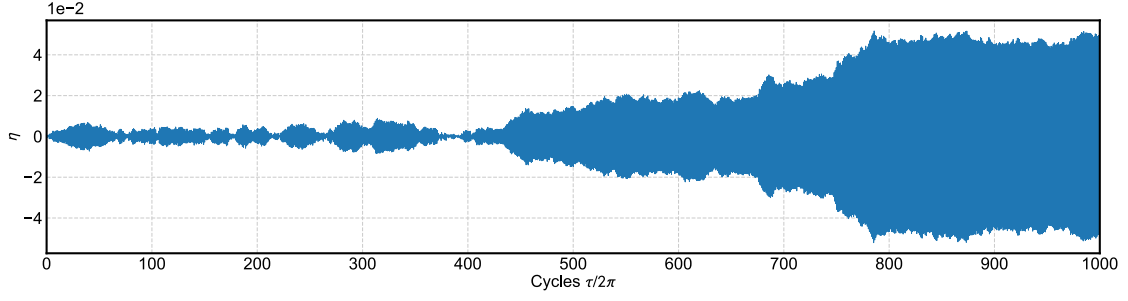


Fig. 15. Realization of VIV time history with stable LCO after random initial conditions for $U = 7.37$ m/s, $\alpha = 7.68^\circ$, $\sigma^2 = 0.01$.

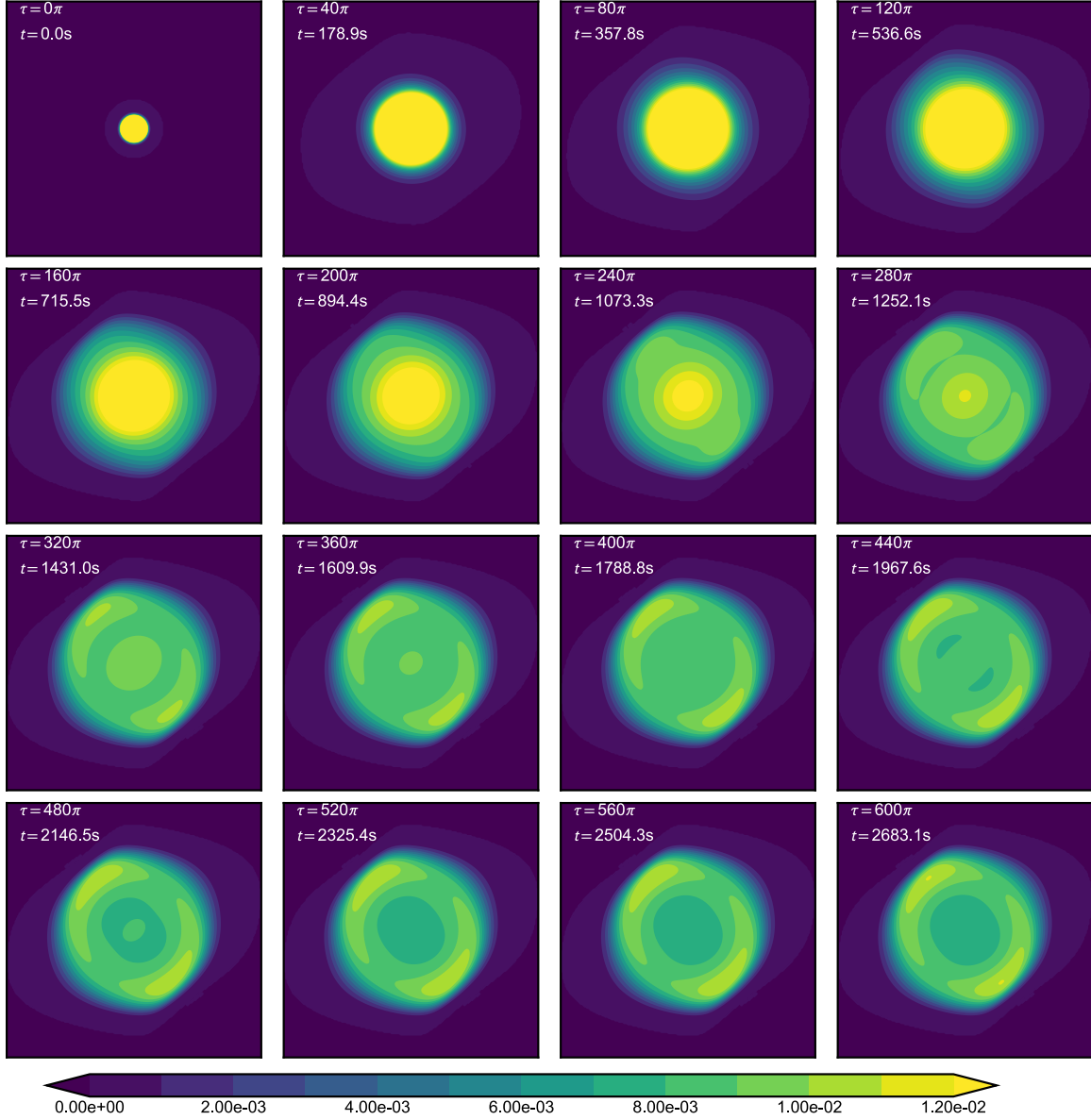


Fig. 16. $p(X, \tau)$ evaluated by FPK equation conditional on $U = 7.37$ m/s and $\alpha = 7.68^\circ$ with intensity $\sigma^2 = 0.01$.

5.5. VIV occurrence probability by FPK equation, conditional on U and α

Combining the nonlinear VIV model with the external excitation as in Eq. (23), the random structural response under nonlinear aeroelastic forces can be simulated. First, numerical integration is employed to simulate the probabilistic VIV events in the time domain. Using the

parameters identified from the first VIV event in Fig. 7 and setting $\sigma^2 = 0.01$ ($\sigma_s^2 = 5 \times 10^{-3}$), the structural responses are calculated and plotted in Fig. 15 with zero initial conditions. Since, in the beginning, responses are small and cannot exceed the unstable equilibrium amplitude in Fig. 12, the aeroelastic forces are not activated. At $\tau/2\pi \approx 400$ the instantaneous response exceeds the unstable equilibrium amplitude,

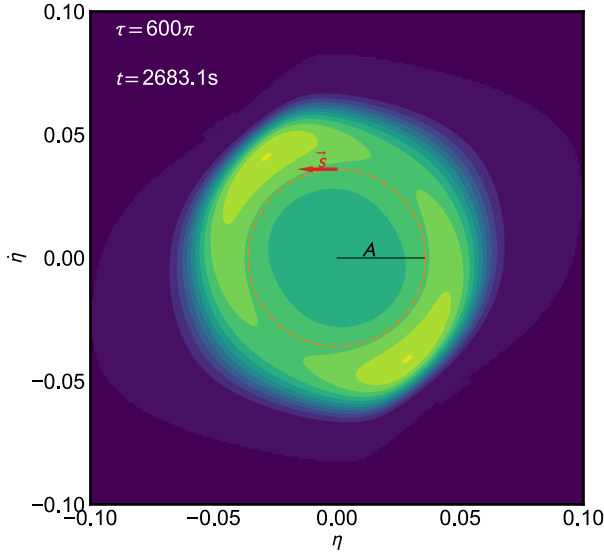


Fig. 17. Probability distribution $p(X, \tau)$ and integral path $S : A = \sqrt{\eta^2 + \dot{\eta}^2}$.

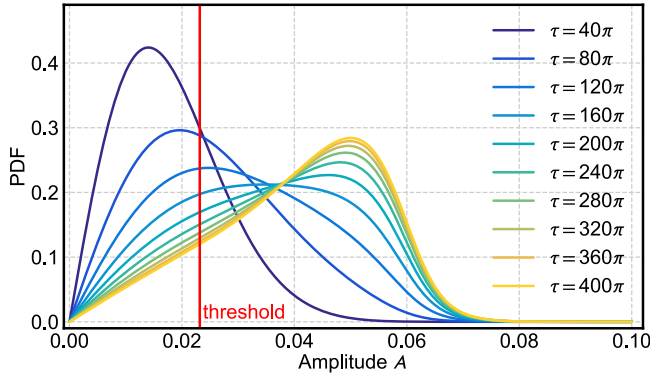


Fig. 18. Probability distribution $p(X, \tau)$ and integral path $S : A = \sqrt{\eta^2 + \dot{\eta}^2}$.

amplitude rate \dot{A} becomes positive and aeroelastic forces are triggered. If $\tau/2\pi > 400$, the response grows until reaching the stable LCO at $\tau/2\pi \approx 800$. The demonstration in Fig. 15 confirms that VIV occurrence is probabilistic rather than deterministic even under uniform, constant U .

In other words, if the duration of VIV-triggering wind conditions is sufficient, the dynamic system will eventually enter VIV and be attracted to the stable LCO amplitude. The FPK equation illustrated in Section 4.1 can be used to evaluate the temporal probability evolution of dynamic states starting from a predefined initial probability $p_0(X) = p(X, \tau = 0)$. The value of $p_0(X) = p(X, \tau = 0)$ is taken from the averaged measurement from non-VIV state during VIV-triggering wind conditions.

For illustration purposes, the probability evolution $p(X, \tau)$ can be numerically calculated by finite differences [33] and is plotted in Fig. 16 by employing the aeroelastic parameters identified from the first VIV event in Fig. 7 with $\sigma_s^2 = 0.005$.

The total duration of the FPK simulations is $\tau = 600\pi$, which is equivalent to $t = 2683.1$ s at full scale. The computational domain is $[-0.12, 0.12] \times [-0.12, 0.12]$, and the finite-mesh elements are 240×240 , the time step is $\Delta\tau = 0.01$ as suggested in [34].

For every $\Delta\tau = 40\pi$ (or $\Delta t = 178.9$ s), the instantaneous $p(X, \tau)$ is plotted in Fig. 16; in this figure the $p(X, \tau)$ within domain $[-0.1, 0.1] \times [-0.1, 0.1]$ are exclusively plotted for better illustration. For $\tau < 160\pi$,

the distribution of $p(X)$ is similar to a bi-variate normal distribution and VIV occurrence is very small. However, for $\tau > 160\pi$ the probability starts to migrate from the center of the contour plot to the stable VIV amplitude locus. For $\tau = 520\pi$, the probability $p(X, \tau)$ at $[0, 0]$ are much lower than $p(X, \tau)$ at the stable VIV amplitude locus; VIV occurrence probability is very high after such a long duration. For $\tau > 520\pi$, $p(X, \tau)$ reaches steady state with most probability concentrated around the LCO circle; once the dynamic system enters the stable LCO, it is less probable to escape from the stable LCO compared to the initial state around $[0, 0]$.

5.6. Probability of response amplitude A and conditional probability $P(V|U, \alpha, \sigma_s)$

The probability of the response amplitude A is the probability “summation” over the all the points, which satisfies the relationship $A = \sqrt{\eta^2 + \dot{\eta}^2}$, expressed as $p(A) = \sum p([\eta, \dot{\eta}] | A = \sqrt{\eta^2 + \dot{\eta}^2})$. In other words, the PDF of A is the path integral of the joint PDF $p(\eta, \dot{\eta})$ on a circular path, whose radius is A , as shown in Fig. 17. More formally, the PDF of A can be written as [35]

$$p(A, \tau) = \oint_S p(X, \tau) d\vec{s} = \oint_{\{S: A = \sqrt{\eta^2 + \dot{\eta}^2}\}} p([\eta, \dot{\eta}], \tau) d\vec{s} \quad (29)$$

Using the circular path integral, the joint PDF of $[\eta, \dot{\eta}]$ is converted to the probability distribution of the response amplitude $p(A)$, which is plotted in Fig. 18. Fig. 18 suggests that, initially, the amplitudes are around the origin, but, as time elapses, the probability $p(A)$ transitions from the origin to a stable LCO amplitude about 4.6. For $\tau > 280\pi$ ($t > 1252.1$ s), the amplitude probability $p(A)$ becomes stable.

However, the duration of stable VIV-triggering wind condition is relatively finite, thus it is necessary to calculate the VIV occurring probability for a certain duration T , which is normally taken as 10 minutes for wind engineering application. The previous VIV threshold is used again here, which is $y_T = 0.048$ m and $A_T = 0.023$ when $U = 7.4$ m/s and plotted as the red line in Fig. 18. Next, the VIV occurrence probability at time T is the summation of $p(A > A_T, \tau = T)$.

$$p(A > A_T, \tau = T) = \int_{A_T}^{\infty} p(A, \tau = T) dA = 1 - \int_0^{A_T} p(A, \tau = T) dA \quad (30)$$

Following the same procedure at various mean wind speeds U and directions α , the VIV occurrence can be evaluated by FPK equations for different ambient excitation intensity σ_s . Fig. 19 depicts the VIV occurrence probability with $\sigma_s \in \{0.1, 0.4, 0.7, 1.0\} \times 10^{-2}$, which clearly indicates that strong excitation increases the VIV occurrence probability since the probability of exceeding the unstable equilibrium amplitude is larger.

For any combination of wind conditions U and α , the VIV occurrence probability can be evaluated by combining the conditional VIV probability using all possible ambient excitation intensities; the PDF of σ_s is determined in Fig. 9. Using the aeroelastic parameters from the first VIV event in Fig. 7 as an example, the VIV occurrence probability $P(V|\sigma_s)$ for $U = 7.37$ m/s, $\alpha = 7.68^\circ$ is plotted in Fig. 20; an exponential function with order 2 (as shown in Fig. 20) is used to fit the FPK results and then multiple with the PDF of $P(\sigma_s)$ to get the overall $P(V|U = 7.37 \text{ m/s}, \alpha = 7.68^\circ)$.

Repeating the above procedure for all mean wind speeds and directions, the $P(V|U, \alpha)$ can be evaluated over the entire range of VIV-triggering wind conditions. The results are shown as the surface plot in Fig. 21. Because of the bridge symmetry in span direction, the $P(V|U, \alpha)$ for $-5^\circ < \alpha \leq 0^\circ$ will be the symmetric copy of $P(V|U, \alpha)$ for $0^\circ \leq \alpha < 5^\circ$.

Fig. 22 shows numbers of observed VIV occurrences and VIV-triggering wind events. The range of VIV-triggering wind conditions is divided into 3-by-3 grids; the VIV event number and wind event number are plotted as 3D histograms. Examining the likelihood of VIV occurrence in the VIV-triggering wind conditions, the observed VIV

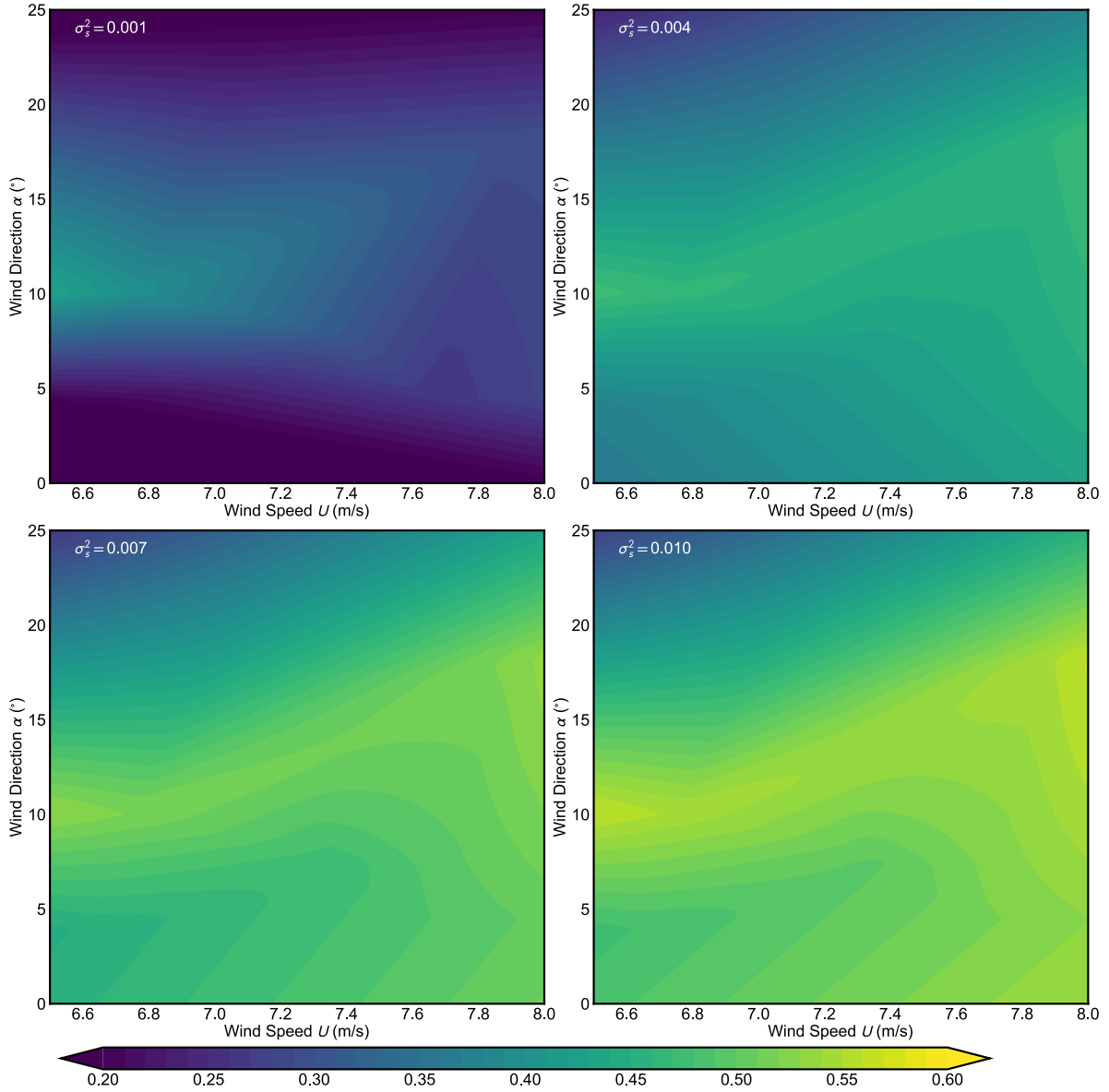


Fig. 19. Contour plots: evaluation of $P(V|U, \alpha, \sigma_s)$ by FPK equations and aeroelastic parameters.

occurrence probability is approximately consistent with the calculated results in Fig. 21. Finally, by combining $P(V|U, \alpha)$ and the wind climate information $P(U, \alpha)$ in Fig. 6(b), the total VIV occurrence probability could be calculated.

5.7. Influence of structural damping on VIV occurrence probability

The evolution of amplitude rate \dot{A} can be determined by Eq. (8). However, the aeroelastic parameters should be re-evaluated for variable damping ξ through Eq. (5). Using the first VIV event in Fig. 7 as an example, Fig. 23 illustrates the relationship between \dot{A} and A for $0.1\% \leq \xi \leq 1.0\%$.

When $\xi = 0.1\%$, the unstable equilibrium amplitude almost vanishes and the amplitude of stable LCO is larger than original damping $\xi = 0.28\%$. As ξ increases, the unstable equilibrium amplitude increases while the stable LCO decreases. For $\xi > 0.8\%$, \dot{A} is negative for all amplitudes A , indicating that VIV will not occur at all under this wind condition.

The VIV occurrence probability is re-evaluated as ξ varies with wind condition $U = 7.37$ m/s, $\alpha = 7.68^\circ$ and ambient excitation $\sigma_s^2 =$

0.004. Because the unstable equilibrium amplitude becomes larger as ξ increases, the VIV occurrence probability rapidly diminishes as ξ increases (see Fig. 24).

Uncertainty in the estimation of modal structural damping of a long-span bridge can be high, especially using SHM methods such as the Bayesian FFT method. Nevertheless, structural damping is combined with the linear part of the aeroelastic damping to yield variable ϵ in Eq. (5). Therefore, uncertainty in structural damping estimation is included with the identification of the aeroelastic parameters through Eq. (28). Thus, the MPV of structural damping was employed as a constant in this study.

6. Concluding remarks

VIV occurrence probability of long-span bridges was re-interpreted by means of wind environment conditions (mean wind speed and directions at deck height). However, field measurements of VIV events on a long-span bridge suggest that, even though wind environment conditions are the same, VIV occurrence is probabilistic rather than deterministic. This study proposed a generalized van-der-Pol model

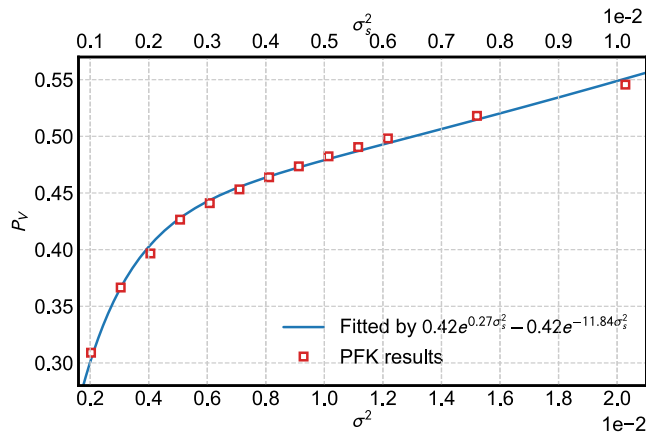


Fig. 20. Conditional VIV occurrence probability $P(V|U = 7.37 \text{ m/s}, \alpha = 7.68^\circ, \sigma_s)$ with variable ambient excitation intensity σ_s .

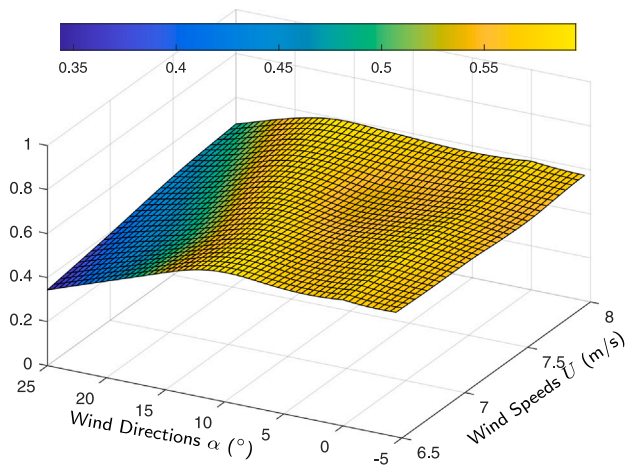


Fig. 21. VIV occurrence probability $P(V|U, \alpha)$ for various VIV-triggering wind conditions.

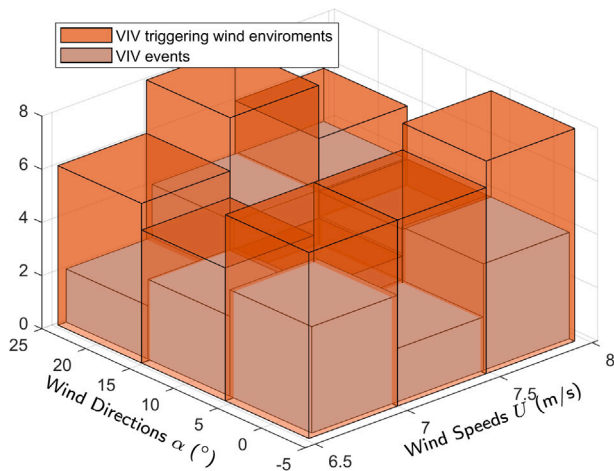


Fig. 22. Three-dimensional histograms of VIV-triggering wind conditions and VIV occurrence events.

and a framework to predict nonlinear aeroelastic effects on bridge decks during sustained VIV with multiple-stability equilibria. The analysis framework consists of three modules:

- (1) wind speed probability distribution at the bridge site;

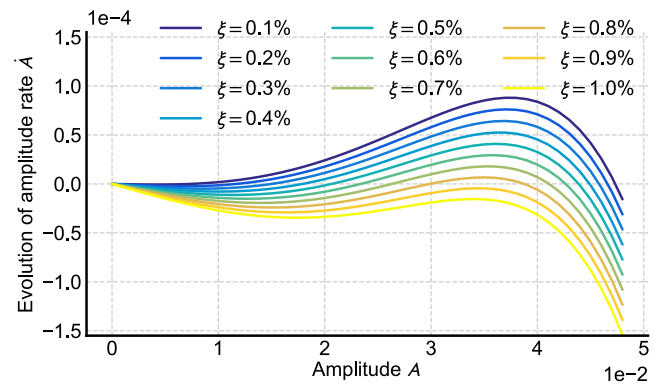


Fig. 23. Evolution of amplitude rate \dot{A} as a function of structural damping ξ when $U = 7.37 \text{ m/s}, \alpha = 7.68^\circ$.

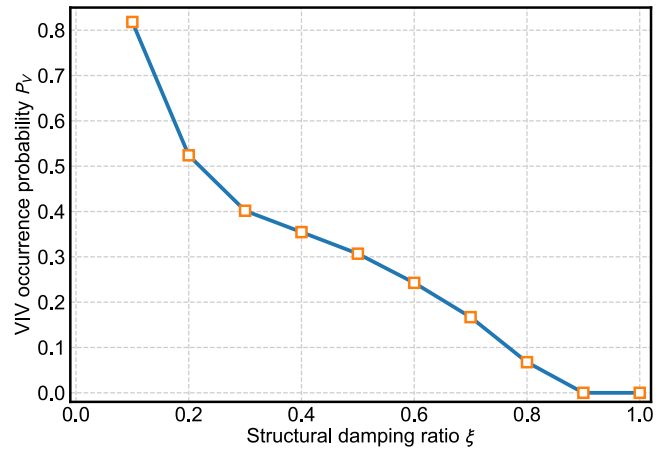


Fig. 24. Decrement of VIV occurrence probability for increasing ξ .

- (2) probability distribution of ambient excitation intensity at the bridge site for VIV-triggering wind conditions;
- (3) VIV occurrence probability under different ambient excitation intensities, evaluated by FPK equation.

The main findings of this paper are:

- (1) if the instantaneous response amplitude is smaller than the 1st unstable equilibrium point, the amplitude tends to diminish to zero; if the instantaneous response amplitude is larger than the 1st unstable equilibrium point, the amplitude tends to grow and approaches the 2nd stable equilibrium point;
- (2) strong ambient excitation intensity amplifies the VIV occurrence probability;
- (3) large modal structural damping of the deck modes decreases the VIV occurrence probability.

Declaration of competing interest

The authors declare that they have no known competing financial interests or personal relationships that could have appeared to influence the work reported in this paper.

Data availability

Data will be made available on request.

Acknowledgments

The authors gratefully acknowledge the support of National Key Research Development Program of China (2021YFF0502200) and National Natural Science Foundation of China (52008314, 52078383). Any opinions, findings and conclusions or recommendations are those of the authors and do not necessarily reflect the views of the above agencies.

References

- [1] Williamson C, Govardhan R. Vortex-induced vibrations. *Annu Rev Fluid Mech* 2004;36:413–55.
- [2] Kumarasena T, Scanlan R, Ehsan F. Wind-induced motions of Deer Isle bridge. *J Struct Eng* 1991;117(11):3356–74.
- [3] Larsen A, Esdahl S, Andersen JE, Vejrum T. Storebælt suspension bridge–vortex shedding excitation and mitigation by guide vanes. *J Wind Eng Ind Aerodyn* 2000;88(2–3):283–96.
- [4] Frandsen J. Simultaneous pressures and accelerations measured full-scale on the Great Belt east suspension bridge. *J Wind Eng Ind Aerodyn* 2001;89(1):95–129.
- [5] Fujino Y, Yoshida Y. Wind-induced vibration and control of Trans-Tokyo Bay crossing bridge. *J Struct Eng* 2002;128(8):1012–25.
- [6] Hwang YC, Kim S, Kim H-K. Cause investigation of high-mode vortex-induced vibration in a long-span suspension bridge. *Struct Infrac Eng* 2020;16(1):84–93.
- [7] Li H, Laima S, Ou J, Zhao X, Zhou W, Yu Y, et al. Investigation of vortex-induced vibration of a suspension bridge with two separated steel box girders based on field measurements. *Eng Struct* 2011;33(6):1894–907.
- [8] Li H, Laima S, Zhang Q, Li N, Liu Z. Field monitoring and validation of vortex-induced vibrations of a long-span suspension bridge. *J Wind Eng Ind Aerodyn* 2014;124:54–67.
- [9] Zhao L, Cui W, Shen X, Xu S, Ding Y, Ge Y. A fast on-site measure-analyze-suppress response to control vortex-induced-vibration of a long-span bridge. *Structures* 2022;35:192–201.
- [10] Wu T, Kareem A. An overview of vortex-induced vibration (VIV) of bridge decks. *Front Struct Civ Eng* 2012;6(4):335–47.
- [11] Hartlen RT, Currie IG. Lift-oscillator model of vortex-induced vibration. *J Eng Mech Div* 1970;96(5):577–91.
- [12] Iwan WD, Blevins RD. A model for vortex induced oscillation of structures. *J Appl Mech* 1974;41(3):581–6.
- [13] Ehsan F, Scanlan RH. Vortex-induced vibrations of flexible bridges. *J Eng Mech* 1990;116(6):1392–411.
- [14] van der Pol B, van der Mark J. Frequency demultiplication. *Nature* 1927;120(3019):363–4.
- [15] Gao G, Zhu L, Li J, Han W. Application of a new empirical model of nonlinear self-excited force to torsional vortex-induced vibration and nonlinear flutter of bluff bridge sections. *J Wind Eng Ind Aerodyn* 2020;205:104313.
- [16] Xu K, Ge Y, Zhao L. Quantitative evaluation of empirical models of vortex-induced vibration of bridge decks through sectional model wind tunnel testing. *Eng Struct* 2020;219:110860.
- [17] Gao G, Zhu L, Han W, Li J. Nonlinear post-flutter behavior and self-excited force model of a twin-side-girder bridge deck. *J Wind Eng Ind Aerodyn* 2018;177:227–41.
- [18] Wang C, Hua X, Huang Z, Tang Y, Chen Z. Post-critical behavior of galloping for main cables of suspension bridges in construction phases. *J Fluids Struct* 2021;101:103205.
- [19] Li S, Li H, Liu Y, Lan C, Zhou W, Ou J. SMC structural health monitoring benchmark problem using monitored data from an actual cable-stayed bridge. *Struct Control Health Monit* 2014;21(2):156–72.
- [20] Yuen K-V, Katafygiotis LS. Bayesian fast fourier transform approach for modal updating using ambient data. *Adv Struct Eng* 2003;6(2):81–95.
- [21] Au S-K. Fast Bayesian ambient modal identification in the frequency domain, part I: Posterior most probable value. *Mech Syst Signal Process* 2012;26:60–75.
- [22] Yuen K-V. Bayesian methods for structural dynamics and civil engineering. John Wiley & Sons; 2010.
- [23] Risken H. The Fokker–Planck equation. Berlin, Heidelberg: Springer; 1996. p. 63–95.
- [24] Náprstek J. Combined analytical and numerical approaches in dynamic stability analyses of engineering systems. *J Sound Vib* 2015;338:2–41.
- [25] Spanos PD, Sofi A, Di Paola M. Nonstationary response envelope probability densities of nonlinear oscillators. *J Appl Mech* 2006;74(2):315–24.
- [26] Canor T, Denoël V. Transient Fokker–Planck–Kolmogorov equation solved with smoothed particle hydrodynamics method. *Internat J Numer Methods Engrg* 2013;94(6):535–53.
- [27] Douglas J. Alternating direction methods for three space variables. *Numer Math* 1962;4(1):41–63.
- [28] Ge Y, Zhao L, Cao J. Case study of vortex-induced vibration and mitigation mechanism for a long-span suspension bridge. *J Wind Eng Ind Aerodyn* 2022;220:104866.
- [29] Johnson RA, Wehrly TE. Some angular-linear distributions and related regression models. *J Amer Statist Assoc* 1978;73(363):602–6.
- [30] Cui W, Caracoglia L. A unified framework for performance-based wind engineering of tall buildings in hurricane-prone regions based on lifetime intervention-cost estimation. *Struct Saf* 2018;73:75–86.
- [31] Cui W, Caracoglia L. Performance-based wind engineering of tall buildings examining life-cycle downtime and multisource wind damage. *J Struct Eng (ASCE)* 2020;146(1):04019179.
- [32] Li S, Laima S, Li H. Cluster analysis of winds and wind-induced vibrations on a long-span bridge based on long-term field monitoring data. *Eng Struct* 2017;138:245–59.
- [33] Kumar P, Narayanan S. Solution of Fokker–Planck equation by finite element and finite difference methods for nonlinear systems. *Sadhana* 2006;31(4):445–61.
- [34] Spencer B, Bergman L. On the numerical solution of the Fokker–Planck equation for nonlinear stochastic systems. *Nonlinear Dynam* 1993;4(4):357–72.
- [35] Cui W, Caracoglia L. Simulation and analysis of intervention costs due to wind-induced damage on tall buildings. *Eng Struct* 2015;87:183–97.